



Tool wear prediction in face milling of stainless steel using singular generative adversarial network and LSTM deep learning models

Milind Shah¹ · Vinay Vakharia¹ · Rakesh Chaudhari¹ · Jay Vora¹ · Danil Yu. Pimenov² · Khaled Giasin³

Received: 31 January 2022 / Accepted: 7 May 2022 / Published online: 20 May 2022
© The Author(s) 2022

Abstract

During milling operations, wear of cutting tool is inevitable; therefore, tool condition monitoring is essential. One of the difficulties in detecting the state of milling tools is that they are visually inspected, and due to this, the milling process needs to be interrupted. Intelligent monitoring systems based on accelerometers and algorithms have been developed as a part of Industry 4.0 to monitor the tool wear during milling process. In this paper, acoustic emission (AE) and vibration signals captured through sensors are analyzed and the scalograms were constructed from Morlet wavelets. The relative wavelet energy (RWE) criterion was applied to select suitable wavelet functions. Due to the availability of less experimental data to train the LSTM model for the prediction of tool wear, SinGAN was applied to generate additional scalograms and later several image quality parameters were extracted to construct feature vectors. The feature vector is used to train three long short-term memory network (LSTM) models: vanilla, stacked, and bidirectional. To analyze the performance of LSTM models for tool wear prediction, five performance parameters were computed namely R^2 , adjusted R^2 , mean absolute error (MAE), root mean square error (RMSE), and mean square error (MSE). The lowest MAE, RMSE, and MSE values were observed as 0.005, 0.016, and 0.0002 and high R^2 and Adj. R^2 values as 0.997 are observed from the vibration signal. Results suggest that the stacked LSTM model predicts the tool wear better as compared to other LSTM models. The proposed methodology has given very less errors in tool wear predictions and can be extremely useful for the development of an online deep learning tool condition monitoring system.

Keywords Tool condition monitoring (TCM) · Milling · Industry 4.0 · SinGAN · Deep learning · Stacked LSTM

✉ Vinay Vakharia
Vinay.Vakharia@sot.pdpu.ac.in

✉ Khaled Giasin
Khaled.giasin@port.ac.uk

Milind Shah
Milind.smtmd20@sot.pdpu.ac.in

Rakesh Chaudhari
rakesh.chaudhari@sot.pdpu.ac.in

Jay Vora
vorajaykumar@gmail.com

Danil Yu. Pimenov
danil_u@rambler.ru

¹ School of Technology, Pandit Deendayal Energy University, Gandhinagar 382007, Gujarat, India

² Department of Automated Mechanical Engineering, South Ural State University, Lenin Prosp. 76, 454080 Chelyabinsk, Russia

³ School of Mechanical and Design Engineering, University of Portsmouth, Portsmouth PO1 3DJ, UK

1 Introduction

Stainless steel alloys are widely used in many industrial fields such as automotive, aerospace, and medical. However, machining of stainless steel possesses a lot of challenges and difficulties. This is due to the tendency of work hardening, low thermal conductivity, and high strength. These are very hard materials which are difficult to machine and result in poor surface finish, tool failure, and irregular wear. The presence of a build-up edge increases tool wear rate and deteriorates the surface integrity of the work. Face milling of stainless steel can solve these difficulties. Milling is a common and efficient machining operation employed in modern industrial manufacturing for fabricating various mechanical parts, such as flat surfaces, grooves, threads, and other complex geometric shapes [1]. Cutting tools are key components in machine milling operations that are inevitably subject to wear during milling and therefore present conditions that vary over their effective lifetimes. Machining

is a vital material removal technique in manufacturing that requires significant attention owing to the time and money required. As the applications for these machines expand, a system for monitoring tool wear becomes important. Tool condition monitoring (TCM) is an important technology in automated manufacturing processes because it increases productivity by reducing downtime, reduces damage to the cutting tool and workpiece, and ensures product quality [2, 3] because a broken tool causes permanent damage to the workpiece's surface. As a result, tool wear affects the machined part surface quality, dimensional accuracy, and operating cost [4, 5]. As a consequence, it is vital to monitor tool wear using direct and indirect methods. The direct method requires the cutting tool to be removed from the machine and an optical microscope is generally used to measure wear, whereas the indirect method uses various sensor signals such as acoustic emission (AE), milling force, tool/workpiece vibration, and spindle motor current, to estimate tool wear [6]. Under typical machining conditions, it is noticed that flank wear is the most prevalent. The width of flank wear (VB) is the most commonly used measure to determine the cutting tool life [7]. This may be quantified directly [6] or indirectly (using sensors). Direct inspection methods include using optical microscopy to examine the condition of the cutting tool edges and measuring the tool wear. However, using this method introduces undesirable interruption periods which slows the machining process and increases the manufacturing costs. On the other hand, the indirect approach makes use of sensors that can monitor the tool wear without interrupting the machining process, therefore reducing the machining time and improving the productivity. Tool condition monitoring is one of the direct methods which are used for determining the value of tool wear without stopping the machining operation [8]. Recent studies have shown an interest in tool wear prediction since this would bring a significant benefit to the industry when it comes to waste reduction, production cost, and accuracy [9]. The typical machine downtime due to tool wear is between 7 and 20% [3]. Numerous methods have been developed in the recent two decades to quantify tool wear, including the use of outputs from acoustic emission sensors, vibration sensors, and current sensors [10, 11]. From the data collected by these sensors, it is possible to estimate tool wear, allowing for a more efficient machining process. A handful of research have been conducted to establish a link between machining parameters and tool wear using the indirect approach of tool condition monitoring [12, 13]. Vakharia et al. [14], for instance, employed Symlet wavelets to extract statistical characteristics from vibration and acoustic emission signals to estimate tool wear. To characterize the acoustic emission (AE) signals captured during cutting, Liang and Dornfeld [15] utilized an autoregressive time series. Their results suggested that detection of tool wear could be accomplished

during machining by monitoring the evolution of the model parameter vector. Mohanraj et al. [16] predicted tool wear in the end milling machining process using wavelet characteristics and Holder's coefficient. The authors analyzed flank wear with vibration signals by implementing various machine learning (ML) algorithms. The confusion matrix was used to analyze the accuracy of ML algorithms and later verified by using benchmarking datasets. The obtained results from the analysis have shown an accuracy of 100% and 99.86% for the support vector machine and decision trees, respectively. Tool life estimation is estimated using various approaches starting from mathematical formulation [17] to stochastic modeling [18], to more complex statistical models [19], and recently, the application of various AI algorithms. Machine learning (ML) algorithms which is a subset of AI techniques can bring automation in a variety of machining tasks, without much involvement of humans. In ML, various models, like SVM, ANN, KNN, etc., initially learn and trained through input data and output data and later can be used for prediction for unseen data [20–22].

Data-driven TCM has grown significantly as the need to incorporate automation and Industry 4.0 in manufacturing industries increases. Furthermore, with more inclusions of multi-sensors, sensor networks, and complex and unstructured data, big data poses a challenge for developing robust models. At present, deep learning (DL) serves as a bridge that efficiently connects big data coming from machinery with intelligent machine condition monitoring techniques. DL is another type of ML algorithm and has been applied in a variety of applications, since 2006. It mimics the functionality of ANN and consists of multiple information processing layers which learn the hierarchical representations of data. Recently, Serin et al. [23] did a comprehensive study about the applications of various deep learning algorithms for TCM. A methodology has been developed for automatic detection of tool wear in the face milling process using convolutional neural network (CNN) that is capable of identifying wear rates with minimal error [24]. Kothuru et al. [25] investigated the application of hyperparameter tuning to improve the accuracy of tool condition monitoring in the face milling process using CNN. Recently, Dzulfikri et al. [26] proposed a deep metric learning approach for stamping tool condition diagnosis. Several DML approaches were examined to see which one was best for determining the state of stamping tools. Authors concluded that the triplet network provided the most favorable results.

Numerous researchers have identified the lack of adequate experimental data to develop machine learning models as a barrier for effective tool condition monitoring and prediction of tool wear. The task becomes challenging when DL models need to be developed as they require large experimental data for training. To overcome this obstacle and to enable effective automation, the

authors developed and investigated the utility of SinGAN for the generation of additional scalograms. Additionally, a thorough review of the literature indicates that prior research has paid little consideration to the prediction of tool wear using a combined approach of wavelet scalograms, SinGAN, and DL models like LSTM. Further authors applied the mother wavelet selection criterion relative wavelet energy (RWE) to select the base wavelet to generate scalograms from acoustic and vibration signals and extract relevant information from image quality parameters and, finally, tool wear has been predicted with various types of LSTM models.

A methodology has been presented related to the generation of additional data. Based on this, the advantage of the proposed method is verified after conducting experiments on publicly available milling datasets from Prognostics Centre of Excellence-Data Repository, NASA [27]. Comparisons of various LSTM models are discussed, and findings are evaluated with the standard performance metrics to determine the efficacy of models for prediction of tool wear. The remainder of the article is structured as follows. In Sect. 2, relevant information related to the experimentation and utilization of SinGAN are described. Section 3 discusses LSTM architecture. In Sect. 4, the

results are described and in Sect. 5 the concluding remarks are highlighted. The methodology of the proposed work can be seen in Fig. 1.

2 Materials and methods

2.1 Workpiece setup and cutting parameters

The experiments were conducted on a milling machine with a varying machining conditions in order to predict tool wear [27]. Cutting speed was set to 200 m/min, the feed rate was varied between 0.25 and 0.5 mm/rev, and cutting depth was varied between 0.75 and 1.5 mm as shown in Table 1. Two types of material, cast iron, and stainless steel J45 were used with an insert of type KC710. The size of the workpieces was 483 mm × 178 mm × 51 mm.

A 70-mm face mill with six KC710 inserts coated with TiC, TiC-N, and TiN for toughness was used in the milling tests. Tool wear was considered and analyzed with three distinct cuts: entrance cut, standard cut, and exit cut. From two locations, i.e., table and spindle, signals were collected using three different types of sensors: acoustic emission, vibration, and current sensor. Among these data, this study

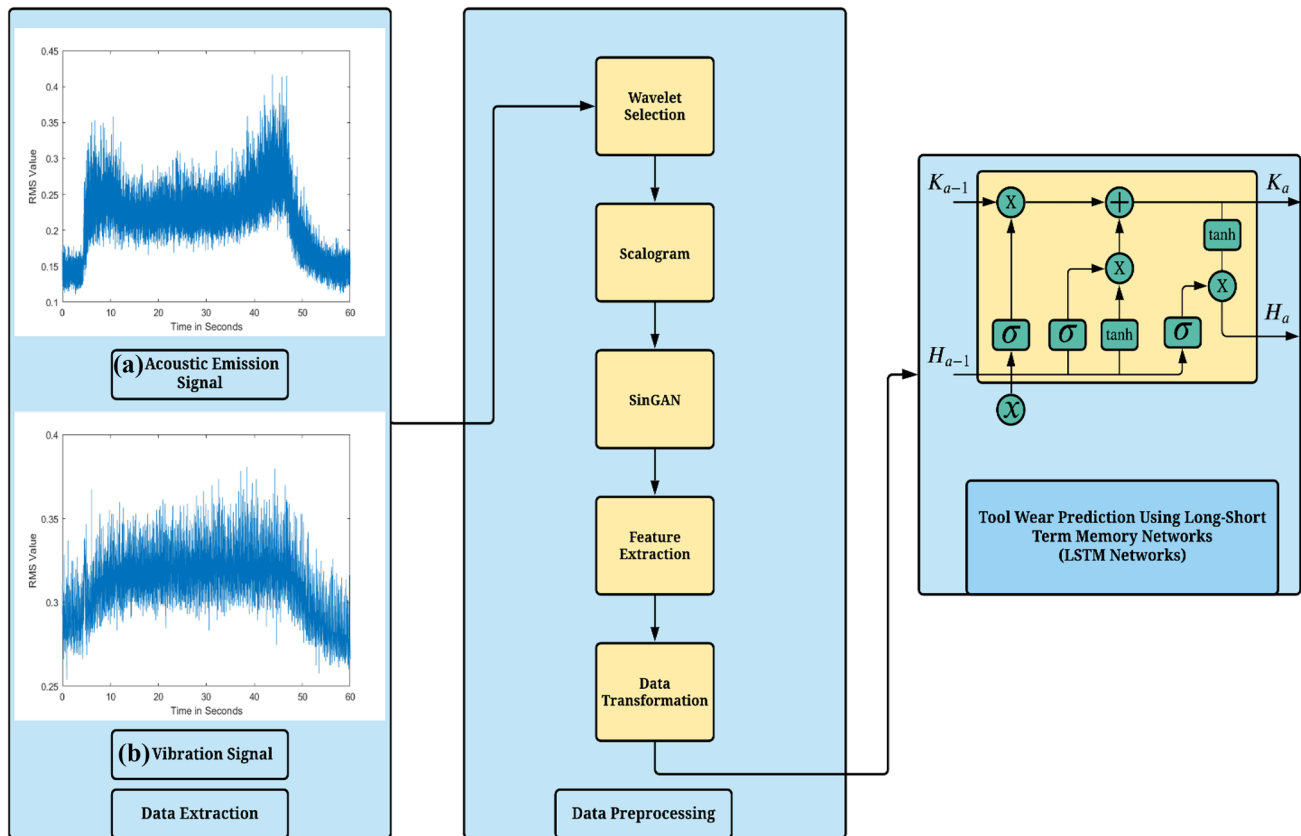


Fig. 1 TCM approach using SinGAN and LSTM

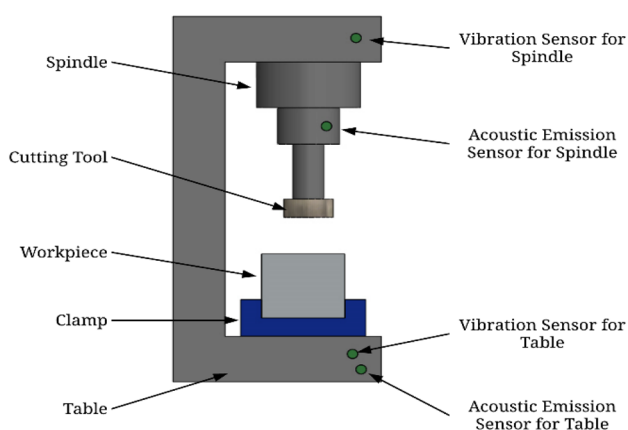
Table 1 Cutting parameters for end milling process

S. no	D.O.C (mm)	Feed (mm/rev)	Cutting speed (m/min)	Material
1	1.5	0.5	200	Cast iron
2	0.75	0.5	200	Cast iron
3	0.75	0.25	200	Cast iron
4	1.5	0.25	200	Cast iron
5	1.5	0.5	200	Cast iron
6	1.5	0.25	200	Cast iron
7	0.75	0.25	200	Cast iron
8	0.75	0.5	200	Cast iron
9	1.5	0.5	200	Steel
10	1.5	0.25	200	Steel
11	0.75	0.25	200	Steel
12	0.75	0.5	200	Steel
13	0.75	0.25	200	Steel
14	0.75	0.5	200	Steel
15	1.5	0.25	200	Steel
16	1.5	0.5	200	Steel

is concentrating on the spindle's vibration and acoustic emission data when milling is performed on a steel workpiece. The experiment was performed 58 times with different cutting parameters, resulting in the generation of 58 AE and 58 vibration signals. The milling machine's schematic diagram is shown in Fig. 2. Table 1 shows the cutting parameters for the end milling process used in the current study.

2.2 Vibration and acoustic signals

Depending on the quality of the cutting tool, vibration levels might vary greatly throughout the machining process. Work-holding or tool-holding devices in one or more directions are the primary focus of the vibration. Vibration data for this experiment were collected using a vibration sensor

**Fig. 2** Schematic diagram of milling machine

attached to the spindle of a Matsuura MC-510 V milling center. The accelerometer was used to detect vibrations (model 7201–50, ENDEVCO). The signal was routed via a Phoenix contact cable connection and amplified and filtered using LP/HP filters before being calculated and entered into the computer for data collection. Acoustic emission (AE) is the spontaneous release of transitory elastic stress energy during the deformation of a material. Acoustic emission data were collected for this experiment utilizing an acoustic emission sensor (model WD 925, Physical Acoustic Group) with a frequency range of up to 2 MHz. This sensor was secured using clamping support. The signal was linked to the terminal of a preamplifier (model 1801, Dunegan/Endevaco) fitted with a high-pass filter set to 50 kHz, and then amplified by a dual amplifier (model DE 302A). The signal is routed via a custom-designed RMS meter and then through a cable to a high-speed data collection board (MIO-16). Figure 3 shows the vibration and acoustic signals captured through various sensors.

2.3 Selection of mother wavelet

To effectively predict the tool wear from the signals, wavelet transform (WT) was used for pre-processing of signals and to generate scalograms. Wavelet is a short wave that is symmetrical and has a mean value of 0. WT was formulated to solve the constraints of extracting useful information from non-stationary signals which Fourier transform was not able to do because of fixed window size [28]. Since then, it has been used in a variety of signal processing applications [29, 30]. In contrast to the short-time Fourier transform's windowed representation, the WT produces a smooth representation. As a result, sudden changes and abnormalities as well as similarities can be effectively analyzed from captured signals. WT is analogous to a mathematical microscope in such a way that it can analyze signals at a variety of scales [31].

Based on the comprehensive literature review, the above-mentioned mother wavelets have been chosen for comparison and the wavelet which is giving maximum relative wavelet energy (RWE) has been chosen to generate scalograms. RWE refers to the energy relative with the distinct frequency bands and further can be applied to characterize and identify specific phenomena in both the temporal and frequency domains [32, 33]. For a given signal, RWE is calculated as follows:

$$R = \frac{Y_i}{Y_t} \quad (1)$$

Here, Y_i and Y_t represent the energy content and total energy content of a signal.

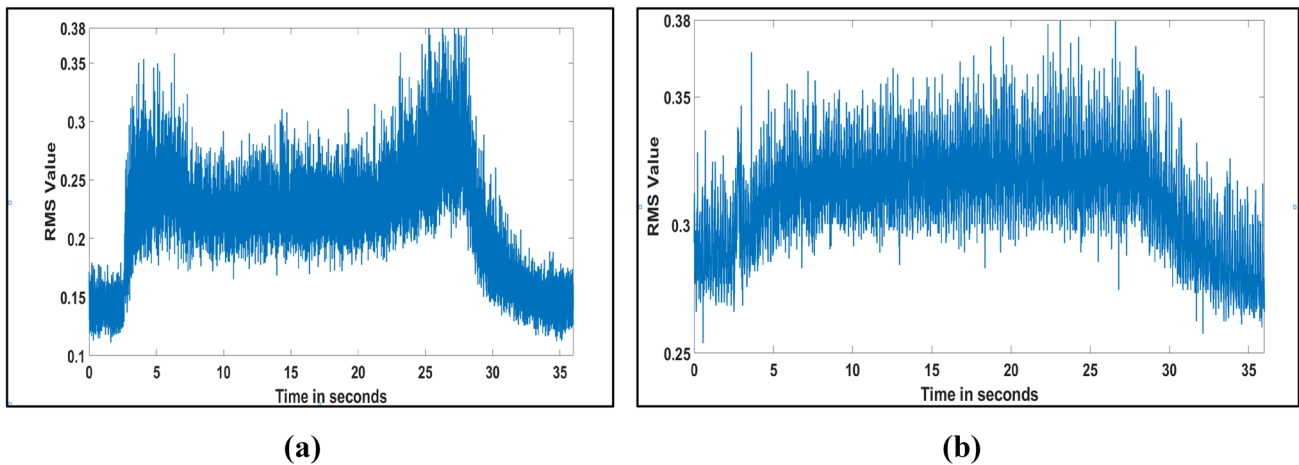


Fig. 3 a Acoustic and b vibration signal at feed = 1.5 mm/rev and depth of cut = 0.5 mm

2.4 SinGAN

When ML or DL models need to be constructed for either classification or regression, the primary issue is the availability of experimental data. The number of experiments conducted for any manufacturing operations is limited, which results in data scarcity. There are several limitations for inadequate data which include associated cost, restrictions in the upper and lower limits of operating parameters, duration of experiments, etc. Thus, to address this issue, and overcome the abovementioned limitations, generative adversarial networks (GAN) are attracting importance in the research community, and it is a type of unsupervised learning. Formulations of new instances from the original data with the applications of GAN are possible in most of the applications as evident from recently published works of literature [34, 35]. GANs have made significant advances in the modelling of high-dimensional distributions of visual data [36]. The goal of GAN is to allow two or more neural networks Generator G and Discriminator D to compete against each other. The Neural Network Generator creates new data instances, while the Neural Network Discriminator examines them for authenticity. When the discriminator is trained, the generator values are maintained constant, and the discriminator values are kept constant when the generator is trained. A duel between the Generator and the Discriminator against a static opponent is used to teach both the Generator and the Discriminator. Following the framework of minmax game, the model can be represented mathematically as [37, 38]:

$$\min_G \max_D V(D, G) = E_{x \sim p_{data}(x)} [\log D(x)] + E_{z \sim p_z(z)} [\log(1 - D(G(z)))] \tag{2}$$

Here, x represents the input image, E is cross-entropy, z is the latent space G draws samples from, and p represents the respective probability distributions.

In the current study, authors have formulated SinGAN, which is an unconditional image generation approach that can learn from a single natural image [39, 40]. Once trained, SinGAN can generate a wide range of high-quality image samples with different aspect ratios as well as different sizes that are semantically similar to the training image from coarse “0” to fine “4” scale.

2.5 Long short-term memory network

Deep learning approaches have been initially used for video and image analysis. However, the vibration signals or acoustic signals are usually one-dimensional sequential data. It is observed that recurrent neural network (RNN), which is a type of DL algorithm, suffers from short-term memory and also vanishing gradient problems. Layers having small gradients stop learning and, as a consequence, RNNs forget what is seen in longer sequences. LSTM is a kind of RNN that is generally considered more appropriate for sequential data, and as a result, they are frequently utilized in natural language processing and speech recognition [41]. Furthermore, it is also observed that in comparison to conventional RNNs, LSTMs perform better in time series prediction [42]. To circumvent the issue of short-term memory loss, LSTM is used which consists of cells and gates through which the flow of information is regulated. To understand which data information should be kept and which should be discarded, gates in LSTM play a vital role, whereas cell carries relevant information about the data throughout the processing stage. The LSTM cell is controlled by three gates: a forget gate (F_a), an input gate (I_a), and an output gate (O_a) whereas K_a, K_{a-1} , and \widehat{K}_a denote the current, previous, and temporary cell states, respectively, as shown in Fig. 4. A sigmoid activation function of type \tanh is used inside gates which keeps

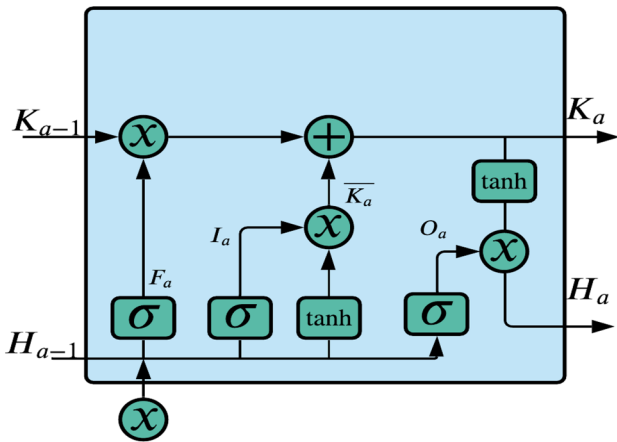


Fig. 4 LSTM cell structure

the values between 0 and 1. The closer value to 0 means forget information, and the closest value to 1 means keep information. The forget gate (F_a), the input gate (I_a), and the output gate (O_a) decide the information that will be discarded from the previous cell, or added to the current cell, and exported from the current cell, with the help of the following equations:

$$F_a = \sigma(W_f \cdot [H_{a-1}, x_a] + B_f) \quad (3)$$

$$I_a = \sigma(W_i \cdot [H_{a-1}, x_a] + B_i) \quad (4)$$

$$O_a = \sigma(W_o \cdot [H_{a-1}, x_a] + B_o) \quad (5)$$

Here, W_f , W_i , and W_o are three weight matrices with respect to forget, input, and output gates respectively. Similarly, B_f , B_i , and B_o are the offset vectors for the forget gate, the input gate, and the output gate. The hidden state H_a of an LSTM cell is computed as:

$$H_a = O_a * \tanh(K_a) \quad (6)$$

whereas σ and \tanh activation functions are computed as follows:

$$\sigma = \frac{1}{1 + e^{-x}} \quad (7)$$

$$\tanh = \frac{e^x - e^{-x}}{e^x + e^{-x}} \quad (8)$$

In our study, we have considered three LSTM models: vanilla LSTM, stacked LSTM, and bidirectional LSTM [43] for in-depth analysis of tool wear prediction for end milling.

3 Results and discussion

To predict tool wear from the end milling process, the authors computed the RWE from different mother wavelets. It has been observed from Table 2 that the Morlet wavelet exhibits maximum RWE for both signals. Fifty-eight scalograms each have been generated from the Morlet wavelet coefficients from both AE and vibration signals, with different operating conditions [44]. Figure 6 illustrates scalograms generated from AE and vibration signals at various scales. In the current study, the authors created 29,000 images (14,500 each from AE and vibration signals) through the Morlet wavelet scalograms which are shown in Fig. 5.

Feature extraction is a process to extract useful information from images. To predict the tool wear with a deep learning network from generated images as seen in Fig. 6, fourteen image quality parameters (IQP) were extracted according to Table 3. Figure 7 shows the feature extraction procedure from scalograms. A feature vector of size $14,500 \times 14$ each was constructed from both AE and vibration scalograms. This feature vector is then fed to deep learning models for training and prediction of tool wear. Long short-term memory network (LSTM), which is a type of deep learning model, is utilized for prediction.

Sample feature vectors are mentioned in Tables 4 and 5 which were constructed from scalograms. As observed from both tables, there are a lot of variations in extracted features. Therefore, the robust transformation of the

Table 2 Maximum relative wavelet energy of different wavelets

Wavelet	Maximum relative wavelet energy for spindle acoustic emission	Maximum relative wavelet energy for spindle vibration
Coiflet1	0.018	0.017
Daubechies1	0.019	0.016
Meyr	0.019	0.017
Morlet	0.021	0.018
Reverse biorthogonal1.1	0.019	0.017
Symlet	0.018	0.017

Fig. 5 Morlet scalograms

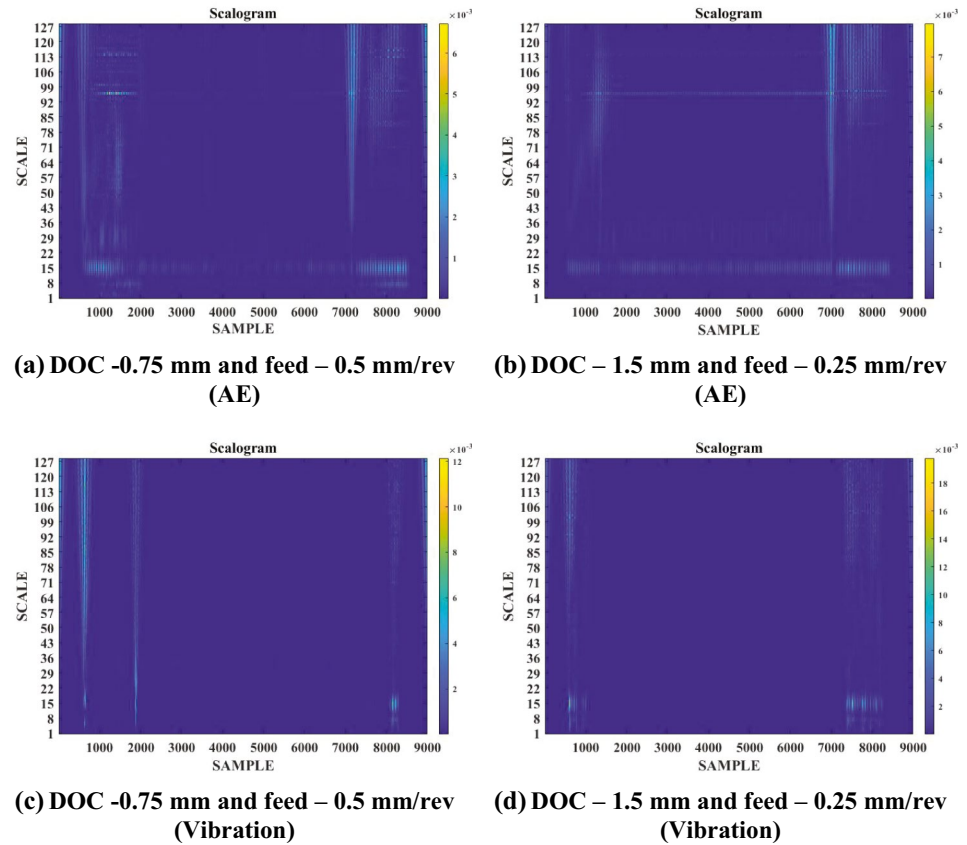


Table 3 Image quality parameters

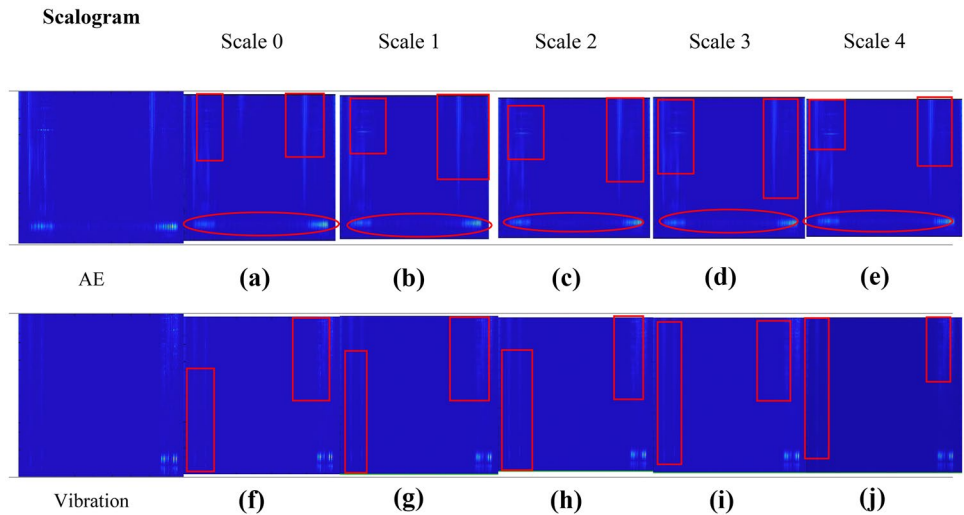
Sr. no	IQP features
1	Structural Similarity Index Measure (SSIM)
2	Chromaticity similarity value (CS value)
3	Mean square error (MSE)
4	Multiscale Structural Similarity Index Measure (MSSIM)
5	Root mean squared error (RMSE)
6	Root mean squared error using sliding window (RMSESW)
7	Relative average spectral error (RASE)
8	Erreur Relative Globale Adimensionnelle de Synthèse (ERGAS)
9	Peak signal to noise ratio (PSNR)
10	Universal Quality Image Index (UQI)
11	Spatial correlation coefficient (SCC)
12	Spectral angle mapper (SAM)
13	Visual information fidelity (VIF)
14	Block sensitive—peak signal-to-noise ratio (PSNRB)

feature vector is needed to reduce the biasedness and to train the LSTM model effectively. In robust feature vector transformation, scaling will be required so that every feature value lies between 0 and 1. It is achieved by subtracting a particular feature column from the median and then dividing it by interquartile range and afterward applied to the full feature vector. The robust transformation was chosen since it is a widely used approach in prediction; Tables 6 and 7 show the sample robust transformed feature vectors. These transformed feature vectors are fed into three different LSTM models namely vanilla LSTM, stacked LSTM, and bidirectional LSTM for prediction of flank wear. To assess the prediction capability, five performance parameters, R^2 , adjusted R^2 , MAE, RMSE, and MSE, were calculated, and formulas are listed in Table 8.

Here, y_r is actual tool wear, y_p is predicted tool wear, \bar{y} is mean of actual tool wear, and N is the total number of observations.

In the current study, 70% of the tool wear features were used for training and the rest (30%) of the tool wear features for testing of the model. Prediction results, from performance metrics, are shown in Fig. 8a–d. It is observed that there are significant variations in values of performance metrics

Fig. 6 a–j Generated scalograms from SinGAN at DOC (0.75 mm) and feed (0.5 mm/rev).



from all LSTM models. In order to further validate the tool wear prediction capability by trained LSTM models, testing of models was carried out and separate plots are included which are shown in Fig. 8b, d. Out of the three LSTMs models, the tool wear prediction error values, i.e., MAE, RMSE,

and MSE, were observed to be very low from AE tool wear feature vector as 0.006, 0.012, and 0.0001, respectively, from the stacked LSTM training model, whereas R^2 and Adj. R^2 values were observed to be 0.998, as shown in Fig. 8a. Similarly, the tool wear prediction error values of MAE, RMSE,

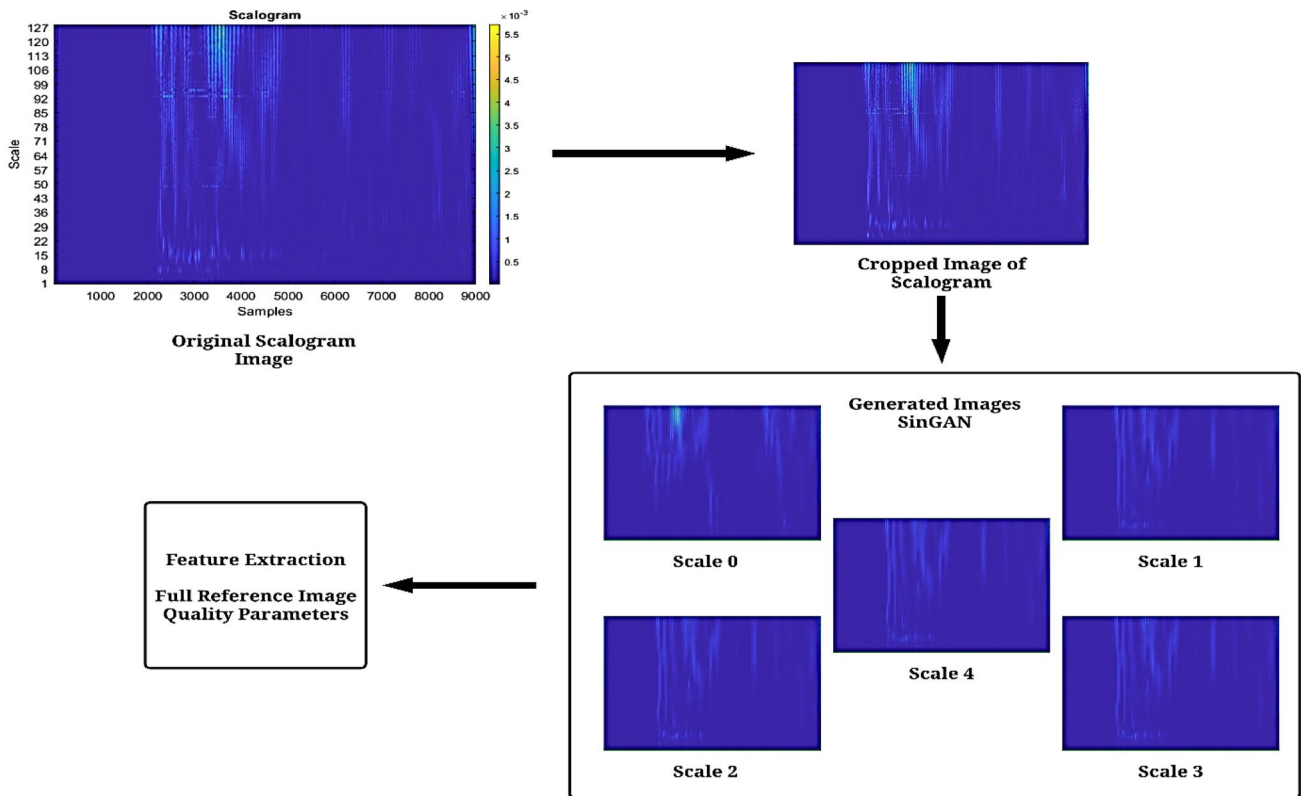


Fig. 7 Feature extraction from scalograms

Table 4 Sample features from AE signals

Sr. no	SSIM	CS value	MSE	MSSIM	RMSE	RMSESW	RASE	ER GAS	PSNR	UQI	SSC	SAM	VIFP	PSNRB
1	0.8952	0.9259	312.3712	0.9715	17.6740	17.4194	1479.834	5919.335	23.1841	0.9343	0.0427	0.0756	0.0903	23.1841
2	0.8967	0.9276	312.9153	0.9713	17.6894	17.4467	1482.276	5929.107	23.1765	0.9341	0.0534	0.0752	0.1063	23.1765
3	0.8947	0.9250	308.4781	0.9709	17.5635	17.3234	1471.954	5887.819	23.2386	0.9351	0.0572	0.0754	0.1054	23.2386
4	0.8904	0.9209	311.5191	0.9671	17.6499	17.4131	1479.060	5916.242	23.1960	0.9343	0.0350	0.0774	0.0973	23.1960
5	0.8920	0.9224	309.6551	0.9691	17.5970	17.3688	1475.559	5902.239	23.2220	0.9348	0.0329	0.0758	0.0970	23.2220
6	0.8909	0.9213	309.3633	0.9689	17.5887	17.3663	1475.201	5900.804	23.2261	0.9346	0.0277	0.0800	0.0872	23.2261
7	0.8926	0.9231	312.7855	0.9710	17.6857	17.4011	1478.024	5912.097	23.1783	0.9345	0.0419	0.0765	0.0941	23.1783
8	0.8934	0.9242	311.6493	0.9674	17.6536	17.4554	1482.745	5930.981	23.1941	0.9340	0.0412	0.0773	0.0907	23.1941
9	0.8929	0.9235	311.6109	0.9685	17.6525	17.4300	1480.620	5922.483	23.1947	0.9341	0.0374	0.0774	0.0951	23.1947
10	0.8907	0.9206	307.7825	0.9674	17.5437	17.2556	1465.860	5863.441	23.2484	0.9356	0.0381	0.0775	0.0936	23.2484
11	0.8931	0.9235	309.5145	0.9689	17.5930	17.3629	1474.839	5899.358	23.2240	0.9347	0.0523	0.0771	0.1004	23.2240
12	0.8944	0.9244	307.0365	0.9681	17.5225	17.2513	1465.449	5861.798	23.2589	0.9356	0.0460	0.0758	0.1035	23.2589
13	0.8929	0.9230	306.6827	0.9692	17.5124	17.2786	1467.945	5871.783	23.2639	0.9354	0.0356	0.0770	0.0975	23.2639
14	0.8893	0.9197	311.9580	0.9656	17.6623	17.3947	1477.243	5908.971	23.1898	0.9344	0.0330	0.0788	0.0830	23.1898
15	0.8937	0.9239	308.3911	0.9683	17.5611	17.2998	1469.816	5879.266	23.2398	0.9353	0.0430	0.0759	0.0968	23.2398

Table 5 Sample features from vibration signals

Sr. no	SSIM	CS value	MSE	MSSIM	RMSE	RMSESW	RASE	ER GAS	PSNR	UQI	SSC	SAM	VIFP	PSNRB
1	0.9547	0.9879	300.0067	0.9927	17.3207	17.2208	1483.103	5932.4142	23.3595	0.9338	0.0333	0.0749	0.3268	23.3595
2	0.9552	0.9888	301.6342	0.9927	17.3676	17.3051	1490.434	5961.7371	23.3360	0.9331	0.0426	0.0763	0.3191	23.3360
3	0.9549	0.9884	299.8952	0.9924	17.3175	17.2618	1486.792	5947.1701	23.3611	0.9334	0.0440	0.0810	0.3500	23.3611
4	0.9544	0.9877	300.9377	0.9922	17.3476	17.2390	1484.730	5938.9206	23.3460	0.9337	0.0383	0.0917	0.3876	23.3460
5	0.9547	0.9883	301.3370	0.9926	17.3591	17.2833	1488.575	5954.3020	23.3403	0.9333	0.0445	0.0861	0.3586	23.3403
6	0.9542	0.9876	300.8992	0.9918	17.3464	17.2551	1486.116	5944.4658	23.3466	0.9335	0.0410	0.0889	0.3605	23.3466
7	0.9555	0.9890	300.9690	0.9930	17.3485	17.2668	1487.182	5948.7294	23.3456	0.9334	0.0429	0.0796	0.3420	23.3456
8	0.9546	0.9882	301.6104	0.9923	17.3669	17.2886	1488.998	5955.9932	23.3363	0.9332	0.0392	0.0865	0.3590	23.3363
9	0.9549	0.9882	300.3795	0.9925	17.3315	17.2288	1483.896	5935.5844	23.3541	0.9338	0.0397	0.0902	0.3863	23.3541
10	0.9552	0.9885	299.1172	0.9927	17.2950	17.2241	1483.558	5934.2355	23.3724	0.9338	0.0446	0.0822	0.3746	23.3724
11	0.9550	0.9881	298.1654	0.9925	17.2675	17.1917	1480.791	5923.1644	23.3862	0.9340	0.0436	0.0852	0.3666	23.3862
12	0.9552	0.9886	300.0177	0.9926	17.3210	17.2564	1486.312	5945.2495	23.3593	0.9335	0.0345	0.0761	0.3328	23.3593
13	0.9546	0.9881	300.9883	0.9923	17.3490	17.2745	1487.842	5951.3705	23.3453	0.9333	0.0441	0.0850	0.3590	23.3453
14	0.9549	0.9883	299.9030	0.9925	17.3177	17.2450	1485.333	5941.3322	23.3610	0.9336	0.0412	0.0823	0.3574	23.3610
15	0.9549	0.9883	301.2826	0.9925	17.3575	17.2536	1485.999	5943.9980	23.3411	0.9335	0.0400	0.0862	0.3545	23.3411

Table 6 Sample robust transformed AE features

Sr. no	SSIM	CS value	MSE	MSSIM	RMSE	RMSESW	RASE	ERGAS	PSNR	UQI	SSC	SAM	VIFP	PSNRB
1	-1.01998	-0.98427	0.119164	-1.54133	0.119951	0.197731	0.339522	0.339522	-0.12072	-0.33401	-1.01482	0.391285	-1.42399	-0.1208
2	-0.96556	-0.9277	0.137216	-1.56052	0.138062	0.245591	0.398751	0.398751	-0.13889	-0.3898	-0.88398	0.380023	-1.31061	-0.13898
3	-1.03738	-1.01322	-0.01001	-1.6104	-0.01011	0.029294	0.148483	0.148483	0.010203	-0.12706	-0.83716	0.38775	-1.31699	0.010224
4	-1.18769	-1.14939	0.090893	-2.06087	0.091556	0.186572	0.32077	0.32077	-0.09221	-0.337	-1.10854	0.442139	-1.37404	-0.09226
5	-1.13064	-1.10029	0.029045	-1.81915	0.029301	0.108829	0.235891	0.235891	-0.02955	-0.21238	-1.13422	0.398879	-1.37665	-0.02956
6	-1.17122	-1.13661	0.019364	-1.84824	0.019539	0.10447	0.227189	0.227189	-0.01971	-0.26018	-1.19845	0.512789	-1.44595	-0.01971
7	-1.11138	-1.07628	0.13291	-1.58981	0.133743	0.165478	0.295644	0.295644	-0.13456	-0.28934	-1.02487	0.415819	-1.39695	-0.13464
8	-1.0822	-1.04083	0.095211	-2.03299	0.095895	0.260778	0.410113	0.410113	-0.09657	-0.41731	-1.03325	0.439216	-1.42079	-0.09663
9	-1.10085	-1.06158	0.093936	-1.89352	0.094615	0.216234	0.358603	0.358603	-0.09528	-0.37979	-1.07941	0.44085	-1.38967	-0.09534
10	-1.17786	-1.15976	-0.03309	-2.034	-0.03343	-0.08967	0.000709	0.000709	0.03377	0.004422	-1.07019	0.44554	-1.40026	0.033808
11	-1.09213	-1.0628	0.024378	-1.84439	0.024595	0.098567	0.218425	0.218425	-0.02481	-0.22581	-0.8976	0.4324	-1.35234	-0.02482
12	-1.04645	-1.03222	-0.05784	-1.94873	-0.05847	-0.09709	-0.00925	-0.00925	0.059104	0.008417	-0.97397	0.397429	-1.3305	0.05916
13	-1.09936	-1.07933	-0.06958	-1.81253	-0.07036	-0.04934	0.051276	0.051276	0.071138	-0.05625	-1.1008	0.431709	-1.37307	0.071204
14	-1.22676	-1.18956	0.105454	-2.24818	0.106186	0.154264	0.276699	0.276699	-0.1069	-0.31154	-1.13375	0.480522	-1.47554	-0.10697
15	-1.07098	-1.04867	-0.0129	-1.91907	-0.01302	-0.01213	0.096638	0.096638	0.013149	-0.07771	-1.01048	0.401078	-1.37798	0.013172

Table 7 Sample robust transformed vibration features

Sr. no	SSIM	CS value	MSE	MSSIM	RMSE	RMSESW	RASE	ERGAS	PSNR	UQI	SSC	SAM	VIFP	PSNRB
1	0.273811	0.39698	-0.22674	0.325791	-0.22893	-0.07278	0.2232	0.2232	0.231135	-0.23977	-1.01943	0.355105	-0.52731	0.231135
2	0.312827	0.475412	-0.13009	0.317693	-0.13117	0.304602	0.569219	0.569219	0.132251	-0.56574	-0.81951	0.390622	-0.57759	0.132251
3	0.292096	0.43559	-0.23336	0.255493	-0.23564	0.110897	0.397324	0.397324	0.237926	-0.40211	-0.78966	0.504637	-0.37615	0.237926
4	0.247217	0.37325	-0.17145	0.191521	-0.17298	0.008674	0.299978	0.299978	0.174507	-0.28521	-0.91309	0.76385	-0.13089	0.174507
5	0.27661	0.425137	-0.14774	0.299173	-0.14901	0.207074	0.481483	0.481483	0.150272	-0.46683	-0.77934	0.628666	-0.32039	0.150272
6	0.230224	0.363322	-0.17374	0.088921	-0.17529	0.080545	0.365413	0.365413	0.176843	-0.35893	-0.85396	0.695514	-0.30745	0.176843
7	0.338991	0.488245	-0.1696	0.412295	-0.1711	0.132891	0.415724	0.415724	0.172605	-0.41794	-0.815	0.470846	-0.42836	0.172605
8	0.266043	0.415964	-0.1315	0.209022	-0.1326	0.230586	0.501439	0.501439	0.133693	-0.48521	-0.89237	0.637941	-0.3176	0.133693
9	0.289822	0.41685	-0.2046	0.278051	-0.20652	-0.03728	0.26061	0.26061	0.208437	-0.25795	-0.8836	0.728563	-0.1396	0.208437
10	0.317315	0.446811	-0.27956	0.313235	-0.28247	-0.05819	0.244693	0.244693	0.285399	-0.25794	-0.77722	0.5324	-0.2159	0.285399
11	0.295575	0.409603	-0.33608	0.279571	-0.33985	-0.20317	0.11405	0.11405	0.343647	-0.13136	-0.79791	0.605941	-0.26816	0.343647
12	0.312927	0.456093	-0.22609	0.304693	-0.22827	0.086542	0.37466	0.37466	0.230464	-0.38647	-0.99332	0.384135	-0.48789	0.230464
13	0.263858	0.40836	-0.16845	0.227926	-0.16994	0.167554	0.44689	0.44689	0.171433	-0.4367	-0.78802	0.601263	-0.31778	0.171433
14	0.293533	0.429766	-0.2329	0.271857	-0.23517	0.035567	0.328436	0.328436	0.237453	-0.33484	-0.85074	0.537087	-0.3282	0.237453
15	0.290108	0.427016	-0.15097	0.269882	-0.15227	0.073761	0.359893	0.359893	0.153368	-0.34934	-0.87565	0.630472	-0.34695	0.153368

Table 8 Performance parameters

Performance metric	Formulas	Ideal value
R^2	$1 - \frac{\sum_i (y_p - y_r)^2}{\sum_i (y_p - \bar{y})^2}$	~1
Adjusted R^2	$1 - \left[\frac{(N-1)(1-R^2)}{(N-v-1)} \right]$	~1
Mean absolute error (MAE)	$MAE = \frac{1}{N} \sum_{i=1}^N y_p - y_r $	~0
Root mean square error (RMSE)	$RMSE = \sqrt{\frac{1}{N} \sum_{i=1}^N y_r - y_p}$	~0
Mean square error (MSE)	$MSE = \frac{1}{N} \sum_{i=1}^N y_r - y_p$	~0

and MSE observed with testing of models are 0.008, 0.023, and 0.0005, respectively, with stacked LSTM model, whereas R^2 and Adj. R^2 values are observed to be 0.995 (Fig. 8b), which is significantly high and near the ideal value as mentioned in Table 8. Therefore, stacked LSTM performance is better than bidirectional LSTM and vanilla LSTM models, when AE tool wear features were used for prediction of wear rate. The performance metrics graphs obtained from vibration features are shown in Fig. 8c, d respectively. The lowest MAE, RMSE, and MSE observed for tool wear prediction are 0.005, 0.008, and 0.00005 again with the stacked

LSTM model during training, whereas significantly high values of R^2 and Adj. R^2 were observed as 0.999, which is shown in Fig. 8c. Similarly, the lowest MAE, RMSE, and MSE observed from testing of feature vectors which are used for tool wear prediction are 0.005, 0.016, and 0.0002 with the stacked LSTM model and R^2 and Adj. R^2 was 0.997, which can be observed from Fig. 8d. The performance of the stacked LSTM model to predict the tool wear is superior as compared to that of bidirectional LSTM and vanilla LSTM models with both training and testing as well as with AE and vibration features respectively as evident from the results. The probable reason why the stacked LSTM model works so well for tool wear prediction with robust scalar transformed features is that robust scalar is resilient against possible outliers present in the feature vector extracted through wavelet transform, and the feature vector is transformed in such a way that outliers have no negative influence when the prediction model is built for tool wear prediction. Furthermore, vanilla LSTM utilizes only one LSTM layer, whereas stacked LSTM utilizes many layers, which are connected very well with each other enabling the model to compute information easily which boosts the model’s effectiveness in predicting tool wear values obtained through experimental results. To highlight and justify the utility of proposed methodology, a comparison table (Table 9) has been prepared with the available literature in which various authors have utilized the same dataset.

Table 9 Comparison table with existing literature to highlight the utility of proposed methodology

References	Material of workpiece	Sensors used	Algorithm	RMSE	MAE	R^2
Hanachi et. al [45]	Cast iron	Current sensors	Sipos	0.42	-	0.429
			Adaptive neuro-fuzzy inference system (ANFIS)	0.56	-	0.289
			Regularized particle filter (RPF)	0.22	-	0.086
Yuan et al. [46]	Cast iron and steel	All sensors are considered	CNN	0.0836	0.0671	0.8725
Traini et al. [47]	Cast iron and steel	All sensors are considered	Logistic regression	0.11	-	0.817
			Decision forest	0.123	-	0.781
			Decision jungle	0.116	-	0.813
			Boosted decision tree	0.122	-	0.794
			Neural network	0.11	-	0.821
Cai et al. [48]	Cast iron and steel	All sensors are considered	Temporal encoder deep LSTM	0.0456	0.0322	0.90
Kumar et al. [49]	Cast iron and steel	Vibration	Vanilla LSTM	0.1129	0.091	0.773
			Bidirectional LSTM	0.0982	0.0764	0.8366
			Encoder—decoder LSTM	0.0586	0.0431	0.9489
			Hybrid LSTM	0.0364	0.0258	0.9837
Zhou and Sun [50]	Cast iron and steel	Current sensors	Kernel extreme learning machine (KELM)	0.013	0.0926	-
			Two-layer angle KELM (TAKELM)	0.003	0.0134	-
			Least squares SVM (LS-SVM)	0.012	0.0254	-
Proposed work	Steel	AE and vibration sensors	Vanilla LSTM	0.0472	0.0284	0.9822
			Bidirectional LSTM	0.0663	0.0393	0.9649
			Stacked LSTM	0.0233	0.0090	0.9957

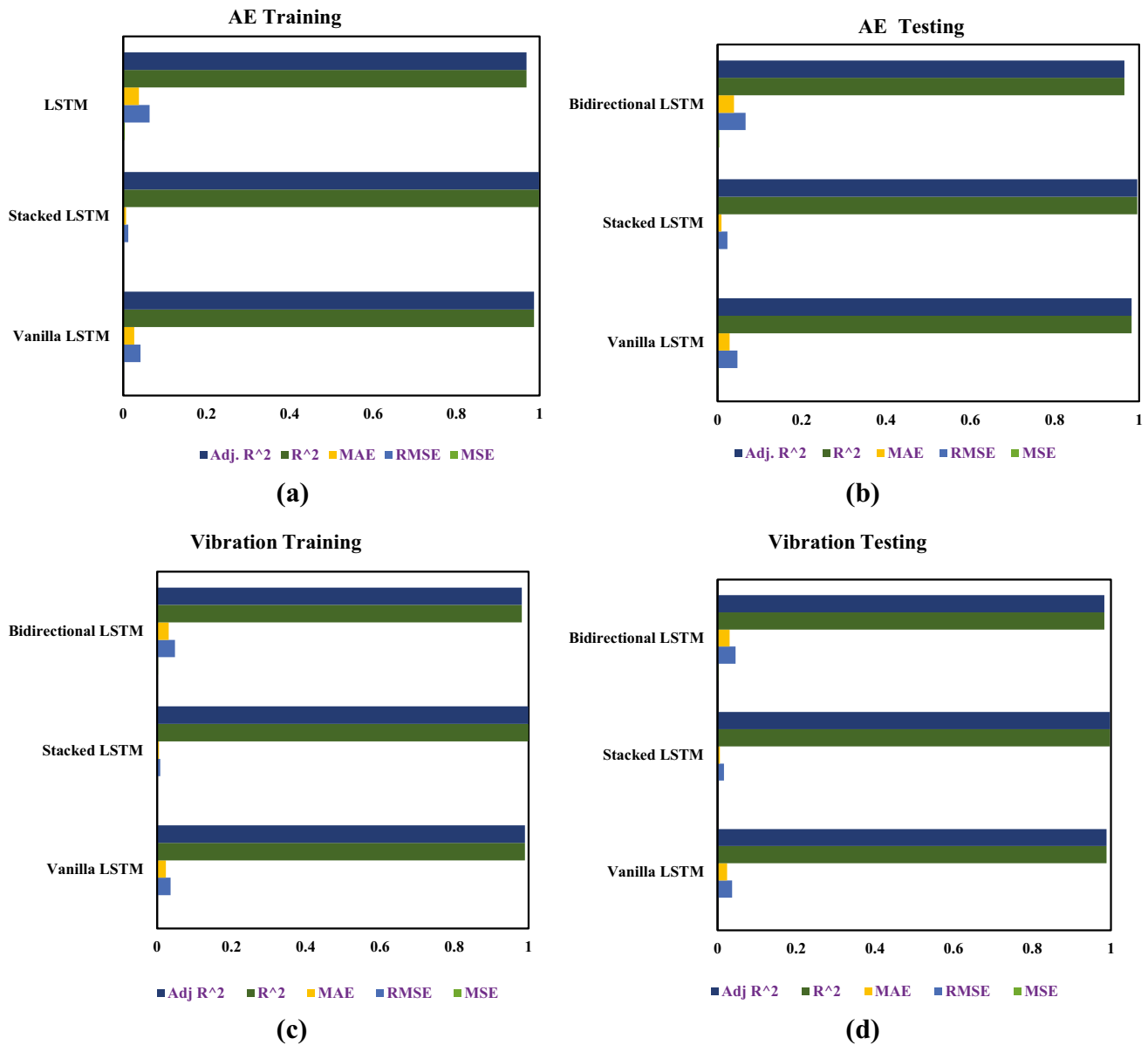


Fig. 8 a–d Performance metric values.

4 Conclusion

In the present paper, a methodology is presented to predict tool wear based on wavelet scalograms, SinGAN, and deep learning models. Initially, 58 scalograms each from AE and vibrations signals were generated from Morlet wavelets and, afterward, SinGAN was applied to generate additional images which are extremely useful to trained LSTM models. Fourteen IQP were extracted to form the feature vector and to randomly split into training and testing. The three models vanilla LSTM, stacked LSTM, and bidirectional LSTM were explored for efficient prediction of tool wear. To analyze the

performance of models, five performance metrics were used, and the outcomes are summarized as follows:

- Tool wear prediction was found to be extremely well from both AE and vibration feature vectors.
- The lowest MAE, RMSE, and MSE values (testing) observed from AE feature vector are 0.008, 0.023, and 0.0005, respectively, whereas from vibration signals 0.005, 0.016, and 0.0002 values (testing) are observed.
- Significantly high R^2 and Adj. R^2 values of 0.997 are observed from the vibration feature vector as compared to 0.995 with the AE feature vector.

- Stacked LSTM predicted tool wear much better as compared to bidirectional LSTM and vanilla LSTM models in case of AE and vibration feature vectors both.
- Superior prediction of tool wear is achieved with the proposed methodology, specifically when the availability of experimental data set is less to train the model.

Availability of data and material The data used in this work can be requested by contacting the corresponding author.

Declarations

Ethics approval Not applicable.

Consent to participate Not applicable.

Consent for publication Not applicable.

Conflict of interest The authors declare no competing interests.

Open Access This article is licensed under a Creative Commons Attribution 4.0 International License, which permits use, sharing, adaptation, distribution and reproduction in any medium or format, as long as you give appropriate credit to the original author(s) and the source, provide a link to the Creative Commons licence, and indicate if changes were made. The images or other third party material in this article are included in the article's Creative Commons licence, unless indicated otherwise in a credit line to the material. If material is not included in the article's Creative Commons licence and your intended use is not permitted by statutory regulation or exceeds the permitted use, you will need to obtain permission directly from the copyright holder. To view a copy of this licence, visit <http://creativecommons.org/licenses/by/4.0/>.

References

- Bustillo A, Pimenov DY, Mia M, Kapłonek W (2021) Machine-learning for automatic prediction of flatness deviation considering the wear of the face mill teeth. *J Intell Manuf* 32(3):895–912. <https://doi.org/10.1007/s10845-020-01645-3>
- Kuntoğlu M, Aslan A, Pimenov DY, Usca ÜA, Salur E, Gupta MK et al (2021) A review of indirect tool condition monitoring systems and decision-making methods in turning: critical analysis and trends. *Sensors* 21(1):108. <https://doi.org/10.3390/s21010108>
- Kuntoğlu M, Aslan A, Sağlam H, Pimenov DY, Giasin K, Mikolajczyk T (2020) Optimization and analysis of surface roughness, flank wear and 5 different sensorial data via tool condition monitoring system in turning of AISI 5140. *Sensors* 20(16):4377. <https://doi.org/10.3390/s20164377>
- Lyu Y, Jamil M, He N, Gupta MK, Pimenov DY (2021) Development and testing of a high-frequency dynamometer for high-speed milling process. *Machines* 9(1):11. <https://doi.org/10.3390/machines9010011>
- Pimenov DY, Bustillo A, Wojciechowski S, Sharma VS, Gupta MK, Kuntoğlu M (2022) Artificial intelligence systems for tool condition monitoring in machining: analysis and critical review. *J Intell Manuf* p. 1–43. <https://doi.org/10.1007/s10845-022-01923-2>
- Mohanraj T, Shankar S, Rajasekar R, Sakthivel N, Pramanik A (2020) Tool condition monitoring techniques in milling process—a review. *J Mater Res Technol* 9(1):1032–1042. <https://doi.org/10.1016/j.jmrt.2019.10.031>
- Silva R, Reuben R, Baker K, Wilcox S (1998) Tool wear monitoring of turning operations by neural network and expert system classification of a feature set generated from multiple sensors. *Mech Syst Signal Process* 12(2):319–332. <https://doi.org/10.1006/mssp.1997.0123>
- Mohamed A, Hassan M, M'Saoubi R, Attia H (2022) Tool condition monitoring for high-performance machining systems - a review. *Sensors* 22(6):2206. <https://doi.org/10.3390/s22062206>
- Pimenov DY, Bustillo A, Mikolajczyk T (2018) Artificial intelligence for automatic prediction of required surface roughness by monitoring wear on face mill teeth. *J Intell Manuf* 29(5):1045–1061. <https://doi.org/10.1007/s10845-017-1381-8>
- Plaza EG, López PN (2018) Application of the wavelet packet transform to vibration signals for surface roughness monitoring in CNC turning operations. *Mech Syst Signal Process* 98:902–919. <https://doi.org/10.1016/j.ymsp.2017.05.028>
- Kuntoğlu M, Salur E, Gupta MK, Sankaya M, Pimenov DY (2021) A state-of-the-art review on sensors and signal processing systems in mechanical machining processes. *Int J Adv Manuf Technol* 116(9):2711–2735. <https://doi.org/10.1007/s00170-021-07425-4>
- Ramesh K, Baranitharan P, Sakthivel R (2019) Investigation of the stability on boring tool attached with double impact dampers using Taguchi based grey analysis and cutting tool temperature investigation through FLUKE-Thermal imager. *Measurement* 131:143–155. <https://doi.org/10.1016/j.measurement.2018.08.055>
- Jumare AI et al (2018) Prediction model for single-point diamond tool-tip wear during machining of optical grade silicon. *Int J Adv Manuf Technol* 98(9):2519–2529. <https://doi.org/10.1007/s00170-018-2402-2>
- Vakharia V, Pandya S, Patel P (2018) Tool wear rate prediction using discrete wavelet transform and K-Star algorithm. *Life Cycle Reliability Safety Engineering* 7(3):115–125. <https://doi.org/10.1007/s41872-018-0057-5>
- Liang S, Dornfeld DA (1989) Tool wear detection using time series analysis of acoustic emission. *J Manuf Sci Eng* 111(3):199–205
- Mohanraj T, Yerchuru J, Krishnan H, Aravind RN, Yameni R (2021) Development of tool condition monitoring system in end milling process using wavelet features and Hoelder's exponent with machine learning algorithms. *Measurement* 173. <https://doi.org/10.1016/j.measurement.2020.108671>
- Taylor FW (1906) On the art of cutting metals. *Am Soc Mech Eng* 23:1856–1915
- Halila F, Czarnota C, Nouari M (2013) Analytical stochastic modeling and experimental investigation on abrasive wear when turning difficult to cut materials. *Wear* 302(1–2):1145–1157. <https://doi.org/10.1016/j.wear.2012.12.055>
- Equeter L, Ducobu F, Rivière-Lorphèvre E, Serra R, Dehombreux P (2020) An analytic approach to the Cox proportional hazards model for estimating the lifespan of cutting tools. *J Manuf Mater Process* 4(1):27. <https://doi.org/10.3390/jmmp4010027>
- Vakharia V, Gupta V, Kankar P (2015) A multiscale permutation entropy based approach to select wavelet for fault diagnosis of ball bearings. *J Vib Control* 21(16):3123–3131. <https://doi.org/10.1177/1077546314520830>
- Bhavsar K, Vakharia V, Chaudhari R, Vora J, Pimenov DY, Giasin K (2022) A Comparative study to predict bearing degradation using discrete wavelet transform (DWT), tabular generative adversarial networks (TGAN) and machine learning models. *Machines* 10(3):176. <https://doi.org/10.3390/machines10030176>
- Bustillo A, Reis R, Machado AR, Pimenov DY (2020) Improving the accuracy of machine-learning models with data from

- machine test repetitions. *J Intell Manuf* 1–19. <https://doi.org/10.1007/s10845-020-01661-3>
23. Serin G, Sener B, Ozbayoglu A, Unver H (2020) Review of tool condition monitoring in machining and opportunities for deep learning. *Int J Adv Manuf Technol* 1–22. <https://doi.org/10.1007/s00170-020-05449-w>
 24. Wu X, Liu Y, Zhou X, Mou A (2019) Automatic identification of tool wear based on convolutional neural network in face milling process. *Sensors* 19(18):3817. <https://doi.org/10.3390/s19183817>
 25. Kothuru A, Nooka SP, Liu R (2019) Application of deep visualization in CNN-based tool condition monitoring for end milling. *Procedia Manuf* 34:995–1004. <https://doi.org/10.1016/j.promfg.2019.06.096>
 26. Dzulfikri Z, Su P-W, Huang C-Y (2021) Stamping tool conditions diagnosis: a deep metric learning approach. *Appl Sci* 11(15):6959. <https://doi.org/10.3390/app11156959>
 27. Agogino A, Goebel K (2007) Milling data set. NASA Ames Prognostics Data Repository, (<http://ti.arc.nasa.gov/project/prognostic-data-repository>), NASA Ames Research Center, Moffett Field, CA
 28. Goupillaud P, Grossmann A, Morlet J (1984) Cycle-octave and related transforms in seismic signal analysis. *Geoexploration* 23(1):85–102. [https://doi.org/10.1016/0016-7142\(84\)90025-5](https://doi.org/10.1016/0016-7142(84)90025-5)
 29. Li C, Wang Y, Ma C, Ding F, Li Y, Chen W et al (2021) Hyperspectral estimation of winter wheat leaf area index based on continuous wavelet transform and fractional order differentiation. *Sensors* 21(24):8497. <https://doi.org/10.3390/s21248497>
 30. Komorska I, Puchalski A (2021) Rotating machinery diagnosing in non-stationary conditions with empirical mode decomposition-based wavelet leaders multifractal spectra. *Sensors* 21(22):7677. <https://doi.org/10.3390/s21227677>
 31. Meyer Y (1992) *Wavelets and Operators*. Cambridge University Press, Cambridge
 32. Rosso O, Figliola A (2004) Order/disorder in brain electrical activity. *Revista mexicana de física* 50(2):149–155
 33. Rosso OA, Blanco S, Yordanova J, Kolev V, Figliola A, et al (2001) Wavelet entropy: a new tool for analysis of short duration brain electrical signals. *J Neurosci Methods* 105(1):65–75. [https://doi.org/10.1016/S0165-0270\(00\)00356-3](https://doi.org/10.1016/S0165-0270(00)00356-3)
 34. Tang T-W, Kuo W-H, Lan J-H, Ding C-F, Hsu H, Young H-T (2020) Anomaly detection neural network with dual auto-encoders GAN and its industrial inspection applications. *Sensors* 20(12):3336. <https://doi.org/10.3390/s20123336>
 35. Wang C, Xiao Z (2021) Lychee surface defect detection based on deep convolutional neural networks with GAN-based data augmentation. *Agronomy* 11(8):1500. <https://doi.org/10.3390/agronomy11081500>
 36. Witmer A, Bhanu B (2022) Generative adversarial networks for morphological–temporal classification of stem cell images. *Sensors* 22(1):206. <https://doi.org/10.3390/s22010206>
 37. Goodfellow I et al (2014) Generative adversarial nets. *Adv Neural Inf Proces Syst* 27. <https://doi.org/10.48550/arXiv.1406.2661>
 38. Akhenia P, Bhavsar K, Panchal J, Vakharia V (2021) Fault severity classification of ball bearing using SinGAN and deep convolutional neural network. *Proc IME C J Mech Eng Sci* p. 09544062211043132. <https://doi.org/10.1177/09544062211043132>
 39. Shaham TR, Dekel T, Michaeli T (2019) SinGAN: learning a generative model from a single natural image. In *Proceedings of the IEEE/CVF International Conference on Computer Vision*. <https://doi.org/10.48550/arXiv.1905.01164>
 40. Vakharia V, Vora J, Khanna S, Chaudhari R, Shah M et al (2022) Experimental investigations and prediction of WEDMed surface of Nitinol SMA using SinGAN and DenseNet deep learning model. *J Mater Res Technol*. <https://doi.org/10.1016/j.jmrt.2022.02.093>
 41. Hao S, Ge F-X, Li Y, Jiang J (2020) Multisensor bearing fault diagnosis based on one-dimensional convolutional long short-term memory networks. *Measurement* 159. <https://doi.org/10.1016/j.measurement.2020.107802>
 42. Sun Q, Tang Z, Gao J, Zhang G (2021) Short-term ship motion attitude prediction based on LSTM and GPR. *Appl Ocean Res* 102927. <https://doi.org/10.1016/j.apor.2021.102927>
 43. Brownlee J (2017) Long short-term memory networks with Python: develop sequence prediction models with deep learning. *Machine Learning Mastery E Book*. <https://machinelearningmastery.com/lstms-with-python/>
 44. Byeon Y-H, Pan S-B, Kwak K-C (2019) Intelligent deep models based on scalograms of electrocardiogram signals for biometrics. *Sensors* 19(4):935. <https://doi.org/10.3390/s19040935>
 45. Hanachi H, Yu W, Kim IY, Liu J, Mechefske CK (2019) Hybrid data-driven physics-based model fusion framework for tool wear prediction. *Int J Adv Manuf Technol* 101(9):2861–2872. <https://doi.org/10.1007/s00170-018-3157-5>
 46. Yuan Y, Ma G, Cheng C, Zhou B, Zhao H et al (2020) A general end-to-end diagnosis framework for manufacturing systems. *Natl Sci Rev* 7(2):418–429
 47. Traini E, Bruno G, D'antonio G, Lombardi F (2019) Machine learning framework for predictive maintenance in milling. *IFAC-PapersOnLine* 52(13):177–182
 48. Cai W, Zhang W, Hu X, Liu Y (2020) A hybrid information model based on long short-term memory network for tool condition monitoring. *J Intell Manuf* 31(6):1497–1510. <https://doi.org/10.1007/s10845-019-01526-4>
 49. Kumar S, Kolekar T, Kotecha K, Patil S, Bongale A (2022) Performance evaluation for tool wear prediction based on Bi-directional, Encoder–Decoder and Hybrid Long Short-Term Memory models. *Int J Qual Reliab*
 50. Zhou Y, Sun W (2020) Tool wear condition monitoring in milling process based on current sensors. *IEEE Access* 8:95491–95502. <https://doi.org/10.1109/ACCESS.2020.2995586>

Publisher's Note Springer Nature remains neutral with regard to jurisdictional claims in published maps and institutional affiliations.